Cellular Dynamics Upon Immune Checkpoint Inhibition

Zhongyang Lin[1], Eketerina Petrenko[1], Mitalee Chandra[2,3], Nalini Srinivas[2,3,4], Selma Ugurel[3,4], Jürgen C. Becker[2,3,4*], & Dvir Aran[1,6*]

[1] Faculty of Biology, Technion-Israel Institute of Technology, Haifa, Israel

[2] Translational Skin Cancer Research, German Cancer Consortium (DKTK), Partner Site Essen, Medical Faculty, University of Duisburg-Essen, Essen, Germany

[3] German Cancer Consortium (DKTK), German Cancer Research Center (DKFZ), Heidelberg, Germany

[4] Department of Dermatology, University Hospital Essen, Essen, Germany

The Taub Faculty of Computer Science, Technion-Israel Institute of Technology, Haifa, Israel.

* Equal last authors

Corresponding author: Dvir Aran

21 Sderot Rose, Technion-Israel Institute of Technology, Haifa, Israel, 3095230

dviraran@technion.ac.il

Keywords: Immunotherapy; Single-cell RNA-seq; Tumor microenvironment; Treatment Response

Abstract

Immune checkpoint inhibitors (ICIs) have revolutionized cancer treatment, still most patients experience limited or no clinical benefit. The immune component dynamics during treatment and how it correlated with treatment efficacy remained largely known. We hypothesize that understanding the modulation dynamics of the TME upon ICI treatment would be key to elucidate the mechanisms of response and resistance. To systematically characterize these dynamics, we aggregated a large-scale single-cell RNA-sequencing (scRNA-seq) dataset of 141 patients across multiple cancer types and ICI treatment modalities, with longitudinally paired samples. We developed a robust, integration-free, and cluster-free deep phenotyping framework, leveraging multiple pan-cancer references to annotate 876,410 high-quality cells into 80 granular cell states. Our analysis revealed consistent compositional changes in 17 cell subtypes following ICI treatment, including an enhanced adaptive immune response such as CD8+ *IL7R*+ central memory T cells, *GZMK*+ effector memory T cells, germinal center B cells, precursor exhausted T cells, and CD4+ TfhTh1 cells, accompanied by a broad reduction in interferon responsive immune cells quiescent CD4+*CREM*- memory T cells. We uncovered co-regulated cell communities within the TME, highlighting the coordinated interplay between adaptive and innate immune cells, as well as immune and non-immune components. Furthermore, we identified two distinct patient groups exhibiting tightly correlated cellular dynamics within the TME post-treatment. The first group, enriched for responders, displayed a marked expansion of naive lymphocytes, while the second group, predominantly composed of non-responders, showed an increased abundance of immune experienced/suppressive cell states. This dichotomy in TME dynamics offers a potential predictive biomarker for patient stratification and personalized therapeutic strategies. Our study presents a comprehensive landscape of the cellular dynamics within the TME during ICI treatment, enabled by a powerful deep phenotyping approach showcasing the importance of a systems-level understanding of the TME dynamics in improving patient stratification and advancing personalized cancer immunotherapy.

Introduction

The tumor microenvironment (TME) is pivotal in shaping the dynamics of tumor progression and immune responses[1-3]. Thus, this intricate network comprising malignant cells, immune cells, and non-immune stromal components, has become a focal point of contemporary therapeutic strategies[4]. These strategies have evolved from targeting cancer cells directly to modulating the immune system, inhibiting angiogenesis, and disrupting the supportive roles of cancer-associated fibroblasts (CAFs). Among these approaches, the emergence of immune checkpoint inhibitors (ICIs) – particularly those targeting the programmed cell death protein 1 (PD1), cytotoxic T-lymphocyte-associated protein 4 (CTLA4) has marked a significant advancement, especially in the treatment of melanoma[5-7].

Despite the notable success of ICIs in increasing survival rates across several cancer types, a significant proportion of patients remain unresponsive to this therapy or develop secondary resistance. For instance, while approximately half of the metastatic melanoma patients experience a long-lasting response to ICIs[8,9], the response rates in cancers like non-small lung cell cancer and renal cell cancer are below 30%[6,10]. Moreover, the treatment is often accompanied by severe adverse effects, with about 60% of melanoma patients experiencing high-grade toxicities, leading to the discontinuation of therapy[6,11,12]. These challenges, coupled with the high costs of ICI treatment, underscore the urgent need for enhanced research tools and methodologies to better predict and understand the varied responses to immunotherapy.

While the clinical success of ICIs validates the potential of immunotherapy, our understanding of the immunological changes they induce remains limited. The current predictive models for ICI response are based on the characteristics of 'hot' tumors, which are rich in T-cell infiltration and pro-inflammatory cytokines, often associated with a high tumor mutational burden (TMB)[13,14]. As the primary target of ICI therapy, CD8+ T cell dynamics are critical factors affecting treatment outcomes. However, these predictors have limited efficacy. With accumulating RNA sequencing data, a pan-cancer analysis revealed that a bulk RNA-seq-derived immune-enriched, non-fibrotic subtype significantly correlates with better ICI response[15]. At the single-cell level, higher abundance of naïve T cells and exhaustion precursor T cells (Texp) have been observed in responsive tumors[16,17]. Despite these findings, the therapy-induced changes in TME cell composition and their potential as predictive biomarkers remain incompletely understood.

Recent studies utilizing site-matched samples from different time points have provided unprecedented insights into the evolving landscape of TME under the influence of ICI. Clonal replacement following PD1 blockade in cutaneous cancer demonstrated limited reinvigoration capacity of T cells[18]. Liu et al. further confirmed the local Texp state after treatment was derived from clonal revival or pre-existing Texp[19]. The emerging 'window of opportunity' for neoadjuvant ICI treatment has facilitated access beyond easy-to-

biopsy cancer types. With a sample collection interval of approximately 9 days, the expanded cytotoxic CD8+T, T helper-1 (Th1), and T follicular helpers (Tfh) cells potentially contribute to response in breast cancer[20]. In triple negative breast cancer, *CXCL13*+ T cells were concurrently expanded alongside pro-inflammatory macrophages and follicular B cells, and this expansion was linked to a positive response during neoadjuvant chemo-ICI combination therapy[21]. A reduction in regulatory T cells (Tregs) was observed in both colorectal and head and neck cancer tumors that achieved pathological complete response[22,23]. Increasing evidence suggest that pre-existing tertiary lymphoid structure (TLS) components consisting of T cells, B cells, and dendritic cells (DC) contribute to response[21,24,25]. Yet, the global TME dynamics upon ICI treatment remain unknown.

The limited number of patients profiled in individual studies and inconsistent cell annotation among them necessitates a broader, more inclusive analysis. Furthermore, scRNA-seq studies typically consider cells from all patients as replications, hindering the examination of variations across patients. To accurately portray the complex landscape of diverse cellular states in TME at an individual patient level, it is imperative to integrate multiple datasets from various cancer types and leverage pan-cancer TME atlases for unified annotation. This approach, coupled with an in-depth analysis of the biological relevance and clinical significance of different cell subtypes within larger patient cohorts, can enhance statistical power, improve the robustness of findings, and pave the way to identify signals that are critical for ICI treatment response.

To accurately portray the complex landscape of diverse cellular states in TME at an individual patient level, we developed a computational framework to integrate multiple datasets from various cancer types and leverage pan-cancer TME atlases for unified annotation. By focusing on sample-level analyses and individual variability in a cohort of 141 patients with pre- and on-ICI treatment scRNA-seq samples, we unraveled the intricate cellular changes that underpin the response to ICI treatment, ultimately contributing to the advancement of personalized cancer immunotherapy.

Results

Large-scale pan-cancer atlas of longitudinally paired ICI-treated tumors

We generated scRNA-seq data from twelve skin cutaneous melanoma patients at day 0 of anti-PD-1 or dual anti-PD1 plus anti-CTLA4 treatment and 7-9 days later (SKCM; Becker). To expand our analysis, we curated a broad range of datasets from 10 recent studies that profiled scRNA-seq from patients at baseline and at a subsequent time point after initiating ICI treatment. This aggregated dataset incorporated profiles from a diverse range of cancer types, including head and neck squamous cell carcinoma [HNSC; Luoma[26],

van der Leun (IMCISION)[22], and Franken[24])], breast cancer (BRCA; Zhang, Bassez[20], and Shiao[25]), colorectal cancer (CRC; Li[23]), prostate cancer (PCa; Hawley[27]), non-small cell lung cancer (NSCLC; Liu [28]), and skin cutaneous basal and squamous cell carcinoma (BCC and SCC; Yost[18]). After rigorous filtering, our assembled cohort comprised 141 patients, each represented by two scRNA-seq time points (**Figure 1A-B and Table S1**).

For 88 patients, the second time point was categorized as 'early on' treatment, i.e., no more than 21 days from treatment initiation, while for the remaining patients, it was designated as 'on/post' treatment, ranging from 28 to 121 days. We collected and curated metadata for all patients, including information on prior treatments, the specifics of the ICI regimen, and various metrics of response to treatment. Patients in the cohort were administered different agents and combinations, which we categorized into monotherapy (anti-PD1/PDL1 with or without chemotherapy; N = 115) and combination therapy (anti-PD1/PDL1 + anti-CTLA4; N = 26). Response metrics varied across studies, including RECIST scores, prognosis (early death after treatment), pathology, and, in some cases, only T-cell expansion levels. We harmonized these diverse response metrics into a binary classification of responders and non-responders (**Methods**). After rigorous quality control at both cell and sample levels, the dataset represented 876,410 cells across 141 samples and 10 cancer types (**Figure 1C**).

To identify granular cell states, we developed a framework for deep phenotyping of the scRNA-seq data. Commonly used integration methods for scRNA-seq data often struggle with strong batch effects, which can distort or dilute the biological signals. Furthermore, conventional clustering methods built on improper integration can lead to impure clusters containing multiple cell types, compromising the purity and interpretability of the data. To circumvent these issues, we employed a two-step solution that minimized the need for data integration. In the first step, we identified the major non-cancer TME components using a complementary combination of clustering by scGate[29] and SingleR[30] (**Figure 1B-D**). The clustering-free second step was particularly advantageous for resolving continuous cell states. Here, we again utilized SingleR, but augmented it with multiple curated references from pan-cancer studies in a hierarchical framework (**Methods**). This allowed us to achieve a high-resolution annotation for each cell, thereby avoiding the pitfalls of clusters derived from integrated embeddings. We first discerned 11 main non-cancer TME components across the 282 scRNA-seq samples (**Figure 1B-D**). The purity and distinctness of these components were confirmed through marker gene validation, ensuring the reliability of our subsequent analyses (**Figure 1E**).

Patient-level Insights into Cellular Dynamics during ICI Therapy

To investigate the impact of ICI treatment on the cellular composition of the TME, we applied linear mixed-effects models (LMMs), which account for the paired nature of the data and allow for the inclusion of the fixed effects (cancer type, timepoint, and treatment modality) and for patients as the random effect for each of the 11 main TME components identified in our analysis. Surprisingly, none of these components showed significant changes in their proportions after treatment (**Figure 1F,G**).

To further explore the functional changes within specific cell types, we utilized curated gene signatures and assessed the functional shifts in CD4+ T cells, CD8+ T cells, and macrophages within pseudo-bulk samples, and applied the LMMs to identify patterns across patients. In both CD4+ and CD8+ T cells, we observed significant changes in several functional programs in response to ICI treatment (**Figure 1H,I**). Notably, we observed significant reduction in interferon response signatures (Effect size (ES)=-0.43, p-value=0.009 and ES=-0.38, p-value=0.027, in CD4+ and CD8+ T-cells respectively) and cytokine/cytokine receptor signatures (ES=-0.65, p-value=0.002 and ES=-0.7, p<0.001, respectively), which may indicate a dampening of the initial inflammatory response following ICI treatment (**Figure 1H**). Interestingly, CD8+ T cells exhibited additional functional changes not observed in CD4+ T cells (**Figure 1I**). These included an increase in anergy (ES=0.86, p-value<0.001), pro-apoptosis (ES=0.78, p-value<0.001), chemokine/chemokine receptor (ES=0.44, p-value=0.013), and exhaustion signatures (ES=0.45, p-value=0.011), suggesting a complex interplay between T cell activation and dysfunction in response to ICI treatment.

Macrophages also underwent significant functional changes in response to ICI treatment, further highlighting the complex dynamics within the TME (**Figure 1J**). We identified a significant increase in phagocytosis (ES=0.91, p<0.001), M2 (ES=0.78, p-value<0.001), MHC class I antigen processing (ES=0.49, p-value=0.013), and angiogenesis (ES=0.45, p-value=0.043), indicating a potential shift towards a more immunosuppressive and tissue-remodeling phenotype. The changes in macrophage function may contribute to the modulation of the TME and influence the overall response to ICI treatment.

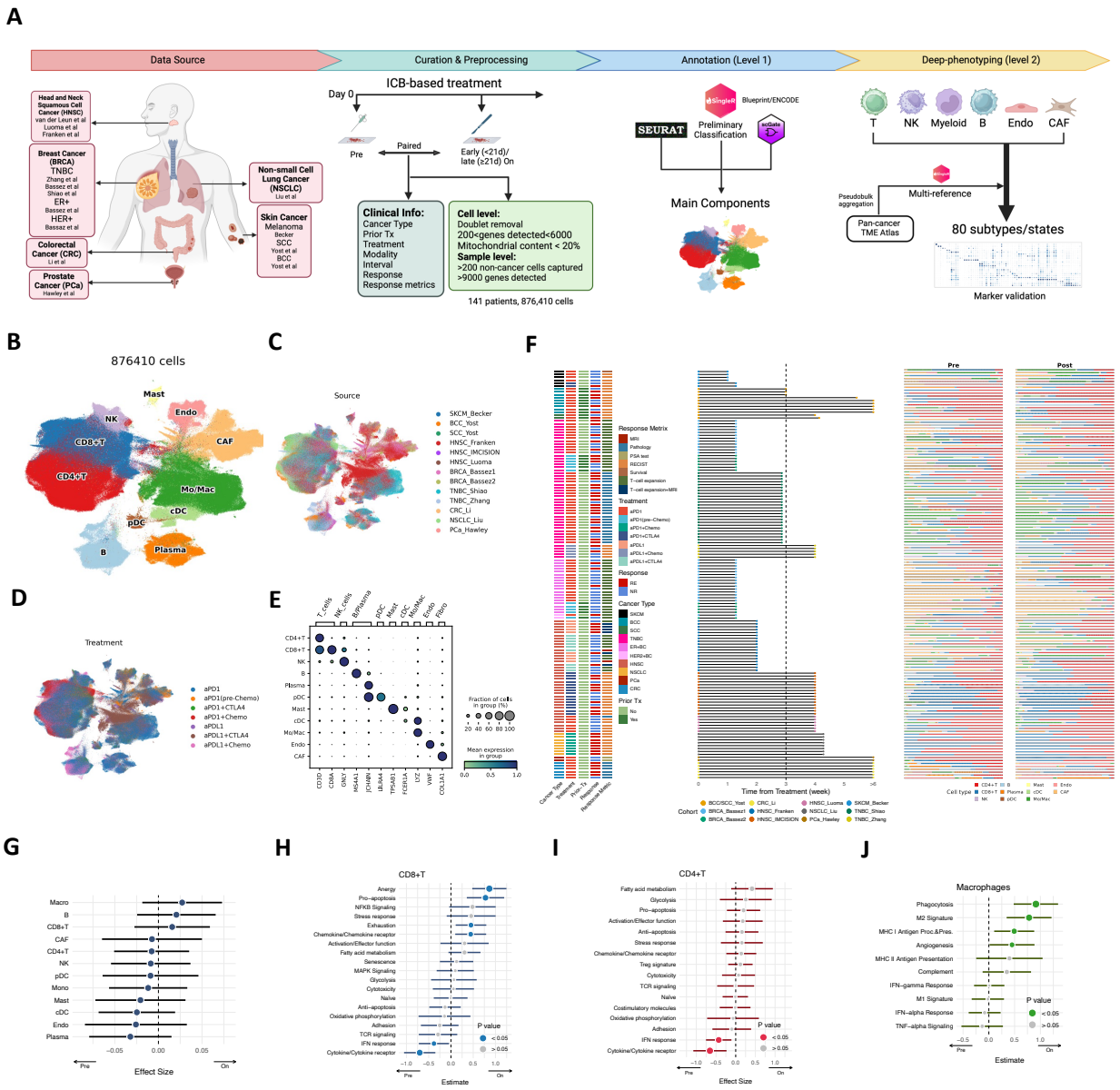

Figure 1. Large-scale pan-cancer atlas of longitudinally paired ICI-treated tumors. A. *Summary of study design and analysis workflow.* ***B-D.*** *UMAP plots showing main components, source, treatment of integrated dataset.* ***E.*** *Dotplot showing marker expression for main components.* ***F.*** *Clinical information and composition of main components by patient.* ***G-J.*** *Forest plots showing the association between main components, pathways (CD4+T, CD8+T, and macrophages) and time points during ICI treatment, the effect sizes (error bars indicate 95% confidence intervals) were based on the coefficients from linear mixed-effects models.*

To gain a more detailed view of the cellular dynamics upon ICI therapy, we applied the hierarchical deep-phenotyping framework for each distinct lineage utilizing a set of specialized references (**Figure 2A and Methods**). This process yielded 80 cell subtypes/states, most of which were represented across datasets (**Figure 2B**). It is noteworthy that some datasets were sorted for specific subsets of TME cells, such as CD3+ cells (Liu and Yost) or CD45+ cells (Hawley, Shiao, Zhang, van der Leun, and Luoma). To validate our deep-phenotyping performance, we employed comprehensive gene markers and curated gene signatures

to validate these cell types and states (**Figure 2C, S1**). Regulatory T cells (Treg) showed a gradient in both regulatory (e.g. *IL2RA, CTLA4, and LAYN*) and costimulatory (*TNFRSF9, TNFRSF18, TNFRSF1B*) signatures, transitioning from an early-phase state towards the activated state (**Figure 2C, S1A**). The recently reported cellular stress signature was predominantly enriched in both CD4+ and CD8+ T cells with high proliferation marker expression (*MKI67* and *TOP2A*), which also exhibited a moderate pro-apoptosis activation (**Figure 2D-E**). Comparatively, T cells in the early phase displayed relatively higher anti-apoptosis activity (e.g. *BIN1, BIN2,* and *BIRC3*) than mature T cells. Macrophages characterized by *C1QC*, *SPP1*, *TREM2*, and *LYVE1* primarily exhibited in anti-inflammatory, M2-like immunosuppressive phenotype, including TGF-beta signaling, MHC I&II antigen processing and presentation, complement, and phagocytosis. Conversely, *INHBA*+ and *IL1B*+ macrophages instead exhibited high expression of genes associated with angiogenesis and inflammatory pathways. *TNF*+ and *FN1*+ macrophages showed activation in both immunosuppression and inflammation, but lacked involvement in angiogenesis and phagocytosis, respectively, demonstrated broad activation across multiple pathways, with particularly strong expression in MHC I antigen presentation, complement pathways, and inflammatory response (**Figure 2C, 2F**). The activated *LAMP3*+ dendritic cells (MigrDC) showed high expression of maturation (e.g. *CD40, CD80, CD86*), regulatory (e.g. *CD274, PDCD1LG2, FAS*), and migratory (e.g. *CCR7, MARCKS, MYO1G*) markers (**Figure 2G**). The atypical memory B cells displayed upregulated maturation, regulatory, exhaustion translation factors (TF), Fc receptors, and activation signatures, compared to naive B cells and memory B cells (**Figure 2H**).

Regarding cellular composition, in line with previous pan-cancer studies, activated regulatory T cells were the most abundant in the CD4+ T-cell compartment, followed by naive and memory CD4+ T cells (**Figure S1B**). Resident memory cells dominated the CD8+ T-cell compartment, followed by early effector memory, naive, and exhausted CD8+ T cells (**Figure S1D**). In B cells, plasma cells were the most abundant, followed by typical memory B cells (**Figure S1F**). The *C1QC*+ macrophages dominated the myeloid compartment (**Figure S1G**). Among non-immune cells, the inflammatory and vascular endothelial cells were most frequently detected (**Figure S1I**). These validations confirmed that our approach can robustly differentiate closely related cell states without the need for data integration and clustering — methods plagued by batch effects and the generation of impure clusters that, while enriched for certain states, are often contaminated with others. It should be noted that attempts to identify these cell states using conventional clustering-based methods were unsuccessful and provided noisy associations with gene markers.

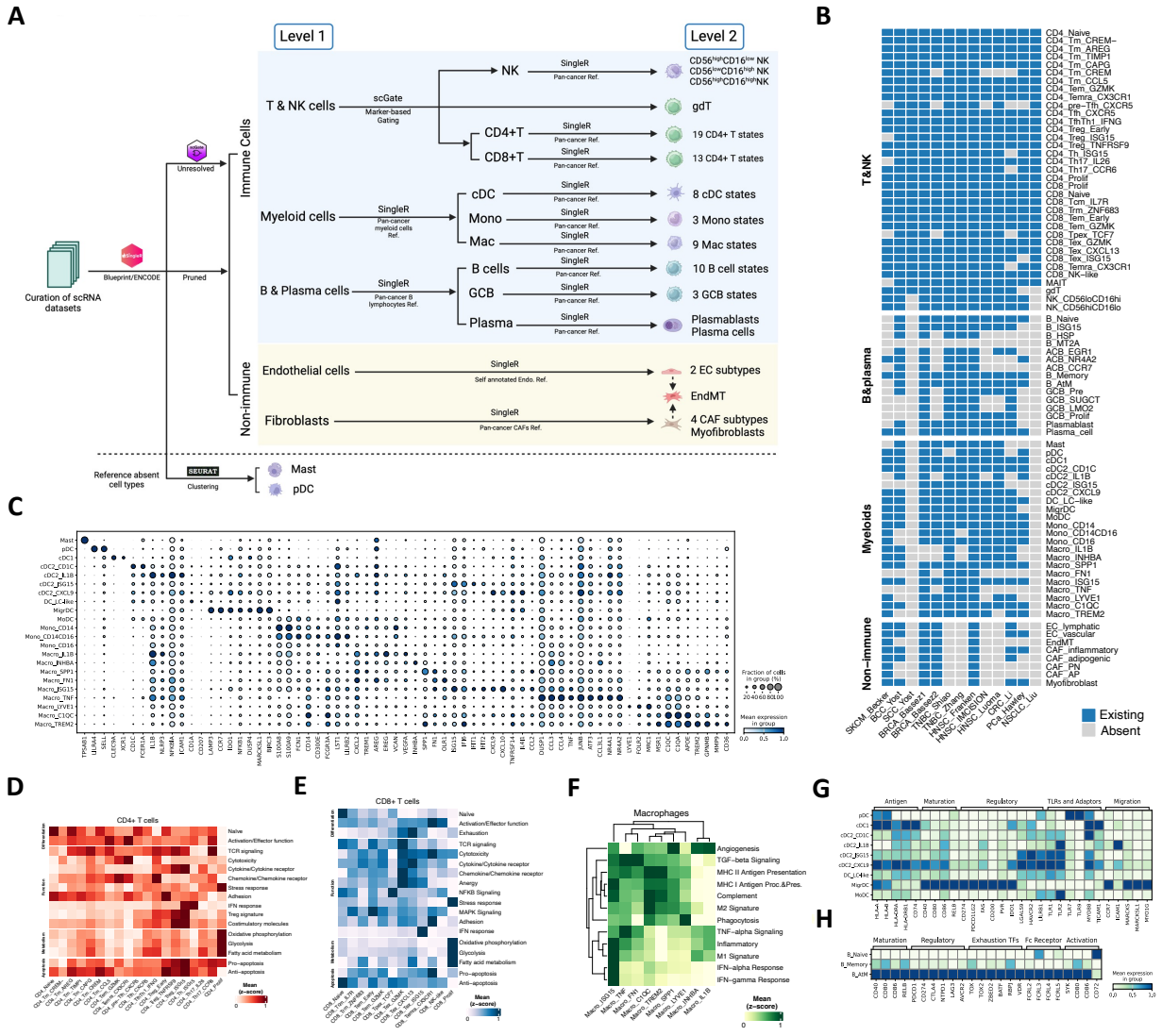

Figure 2. Deep-phenotyping annotation and characteristics. A. *Deep-phenotyping annotation workflow.* ***B.*** *Heatmap showing the presence of cell states/subtypes across datasets. Existing (blue) represents cell types were detected in > 3 samples in a specific cohort, or in at least 1 sample when the cohort has no more than 4 samples.* ***C.*** *Dot plot showing gene expression of myeloid cells. Colors represent relative mean expression (column-wise scaled) of marker genes, and the size represents the percentage of cells expressing these genes.* ***D-F.*** *Heatmaps show curated signatures across CD4+T cells, CD8+T cells, and macrophages.* ***G-H.*** *Heatmaps show relative mean expression (column-wise scaled) selected marker gene expression across conventional dendritic cells and B cells.*

To evaluate the dynamic changes, we applied LMMs to the compositional data, adjusting for potential confounding variables, including sample collection interval, treatment modality, and dataset. This analysis identified 17 cell subtypes that showed significant changes between the two time-points (**Figure 3A-F**). For example, CD8+ Tcm (IL7R+) presented an increase in their frequency in the second time-point in 104 patients compared to only 27 with a decrease (ES = 0.19; p-value < 0.001, **Figure S2B**). Cell subtypes that consistently increased upon treatment included various T and B lymphocyte subsets, such as effector memory T cells, CD4+ TfhTh1 cells, and germinal center B cells (GCB). In contrast, a global reduction in

interferon (IFN) responsive immune cells was observed, primarily affecting T lymphocytes, gamma-delta T cells, and cDC (**Figure 3F**). These cell states, which showed significant increases or decreases post-treatment, exhibited consistent dynamics across most datasets. However, due to low statistical power, they often did not reach statistical significance (**Figure 3B-F**). The concordance observed amongst datasets bolsters our confidence in these findings and emphasizes the enhanced statistical power afforded by our meta-analytical approach.

Interestingly, *CREM*- CD4+ memory T cells, with lowest T cell receptor (TCR) signaling among CD4+T memory cells, which showed significant decrease upon ICI treatment (ES = -0.14; p-value = 0.001), exhibited enhanced gene expression in oxidative stress responses (*TXNIP*), immune signaling regulation (*TRAF3IP3*), gene expression (*MALAT1*), vesicle trafficking (*TBC1D10C*), and cell survival (*GIMAP4*). Alternatively, they show reduced expression in cell proliferation (*RGCC, SRGN, YPEL5*), iron metabolism (*FTH1*), and altered gene regulation (*CREM)* (**Figure S2C**). These cells are characterized by upregulated pathways related to interferon-alpha response and downregulated pathways involved in inflammation, cell proliferation, and metabolism (TNF-alpha Signaling via NF-kB, Myc Targets V1, G2-M Checkpoint, mTORC1 Signaling, E2F Targets, **Figure S2D**). This quiescent yet primed state consistently decreases during ICI treatment, suggesting a shift towards a more active anti-tumor immune response.

Next, to investigate divergent dynamics between ICI regimens, we conducted a subgroup analysis using LMMs to represent general patterns in each treatment modality (**Figure 3G**). Additionally, we performed paired t-tests within treatment-cohort subgroups as an orthogonal validation method (**Figure 3H**). Interestingly, *IL1B*+ and *INHBA*+ macrophages and *CD16*+ monocytes, which are associated with inflammatory and pro-angiogenesis function, decreased in monotherapy but tended to increase in combination therapy. Overall, the paired t-tests revealed consistent trends in cell type dynamics across treatment-cohort subgroups, aligning with the general patterns observed from the LMMs. However, some variations did not reach statistical significance. This consistency suggests that dynamic changes in cell states may reflect a general mechanism of response to ICI therapy, rather than being specific to cancer type or treatment regimen. However, the differing dynamics observed between monotherapy and combination therapy highlight the potential for tailoring immunotherapeutic strategies based on the specific cellular and molecular profiles of the TME.

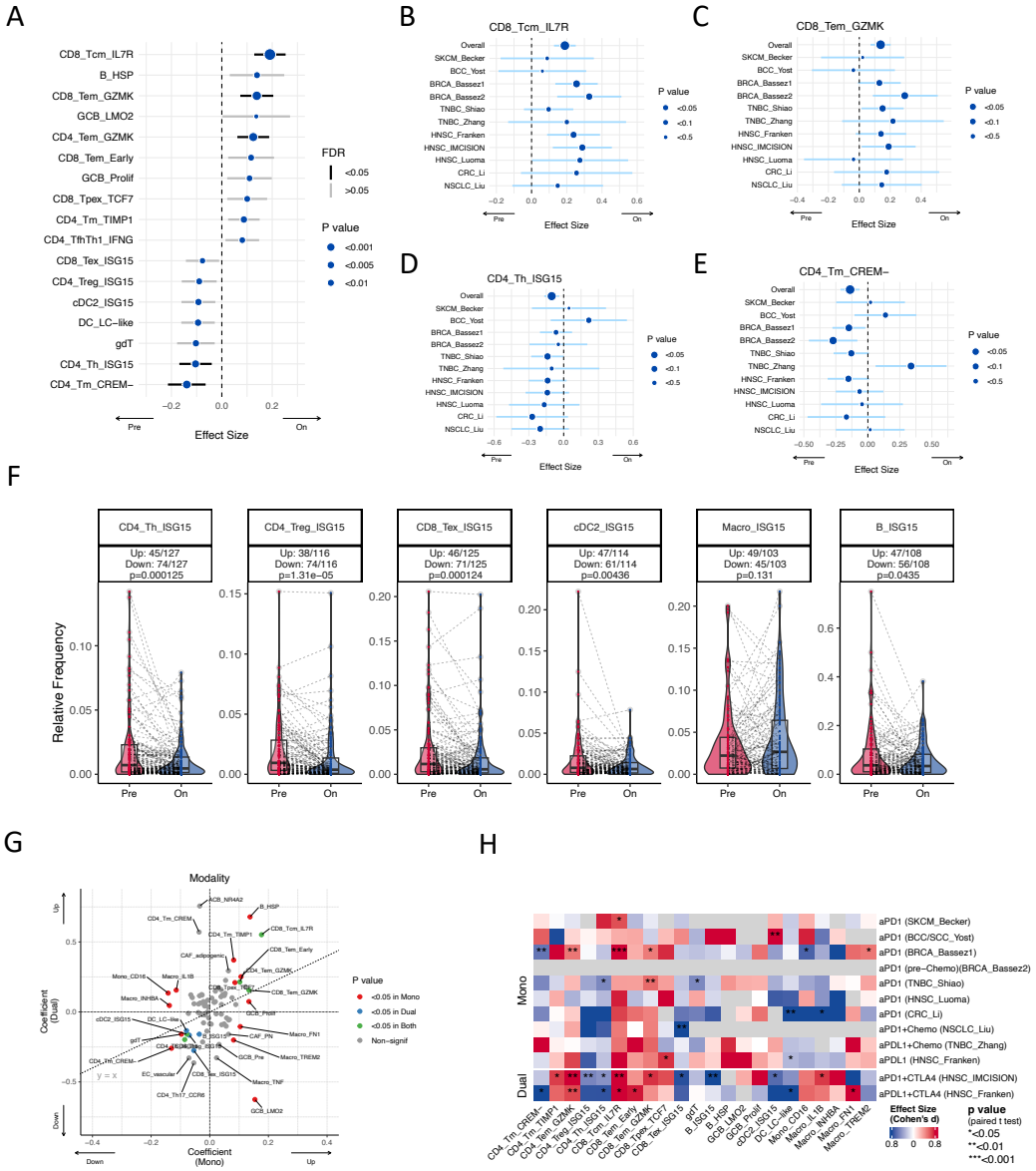

Figure 3. Patient-level compositional analysis. A. *Forest plot for the associations between cellular abundance (relative frequency, RF) and treatment time points.* ***B-E.*** *Forest plots for the associations between cellular abundance (RF) and time points by cohort in selected cell types.* ***F.*** *Paired box and violin plots comparing RF between time points for interferon-inducible gene-enriched cell states. Boxes show 25th, median, and 75th percentiles.* ***G.*** *Effect sizes from subgroups analysis of monotherapy (Mono) treated patients and combination therapy (Dual) treated patients.* ***H.*** *Heatmap showing the effect sizes (Cohen's d) of compositional change for each cell type (column) in modality-cohort subgroups (row), *p<0.05, **p<0.01, ***p<0.001, based on paired Student's t-test. Gray color indicates that the cell type wasn't detected in < 3 patients in the subgroup.*

Co-regulating Patterns upon ICI Treatment

To further elucidate the collective behaviors within the TME and to discern patterns of cellular dynamics in response to ICI therapy, we conducted a pairwise correlation analysis of proportion changes in cell types and states across patients (**Figure 4A,B and S3B**). This analysis was conducted in two iterations: the first

encompassed all patients with available immune cell data (**Figure 4B**), and the second was restricted to patients for whom all TME data was accessible (**Figure S3B**). The correlation analysis unveiled several intriguing groups of cells that exhibited similar dynamics across the patient cohort. These clusters represent groups of cell types and states that, potentially, are co-regulated or are part of a shared response pathway to ICI treatment.

The unsupervised Leiden clustering[31] highlighted inter-lineage cellular communities (**Figure 4C**). An *ISG15*-correlated cell community was identified, reflecting a concomitant interferon response (**Figure 4D**). Notably, the overall change of *ISG15*+ cellular abundance significantly correlated with T cell expansion in breast cancer and head and neck cancer (**Figure 4E**). Within individual cohorts, the overall changes followed the same trend, though the results were not statistically significant (**Figure S3E**). We also identified a cytotoxic community, comprising both adaptive and innate immune response. This community includes cytotoxic NK cells, terminally differentiated effector T cells, gdT cells, and monocytes (*CD14*+ and *CD16*+). Notably, this cytotoxic community showed a strong positive correlation with a naive cell community, which includes naive B cells, CD8+ naive T cells, with CD4+ naive T cells acting as a node connecting the two communities. We also identified an early-phase activation community, involving activated B cells (*NR4A2* and *EGR1*) and CD4+ Tm cells (*AREG*, *CREM*, and *CCL5*), cDC1, CD8+ Tcm cells (*IL7R*), early CD8+ Tem cells, *GZMK*+ CD4+ Tem, and *TNF*+ macrophages. Furthermore, we identified correlations between *TNFRS9*+ Tregs and inflammatory CAFs (**Figures 4F**) as well as between *LYVE1*+ macrophages and adipogenic CAFs (**Figures S3F**), illustrating the co-regulation between immune and non-immune cells.

In the negative correlation graph, a strong negative correlation was observed between plasma cells and naive/memory B cells. Additionally, *C1QC*+ macrophages and CD4+ Tregs, which showed a positive correlation to each other, negatively correlated with both monocytes and naive T cells (**Figure S3A, D**). Collectively, two distinct patterns were observed (**Figures 4D and S3F**): The first TME pattern encompasses cell types pivotal in the early stages of immune response activation, including naive T and B cells, non-switched memory B cells, and dendritic cells, i.e., highlighting a readiness for antigen engagement and initiation of adaptive immune responses; the second TME pattern comprises cell types integral to the modulation of immune activation and the establishment of an immunosuppressive environment. The correlation between these two patterns illustrates a continuum of immune modulation within the TME, from an initial state of readiness through active engagement to a more complex interplay of activation and regulatory suppression, revealing the dynamics in response to ICB therapy.

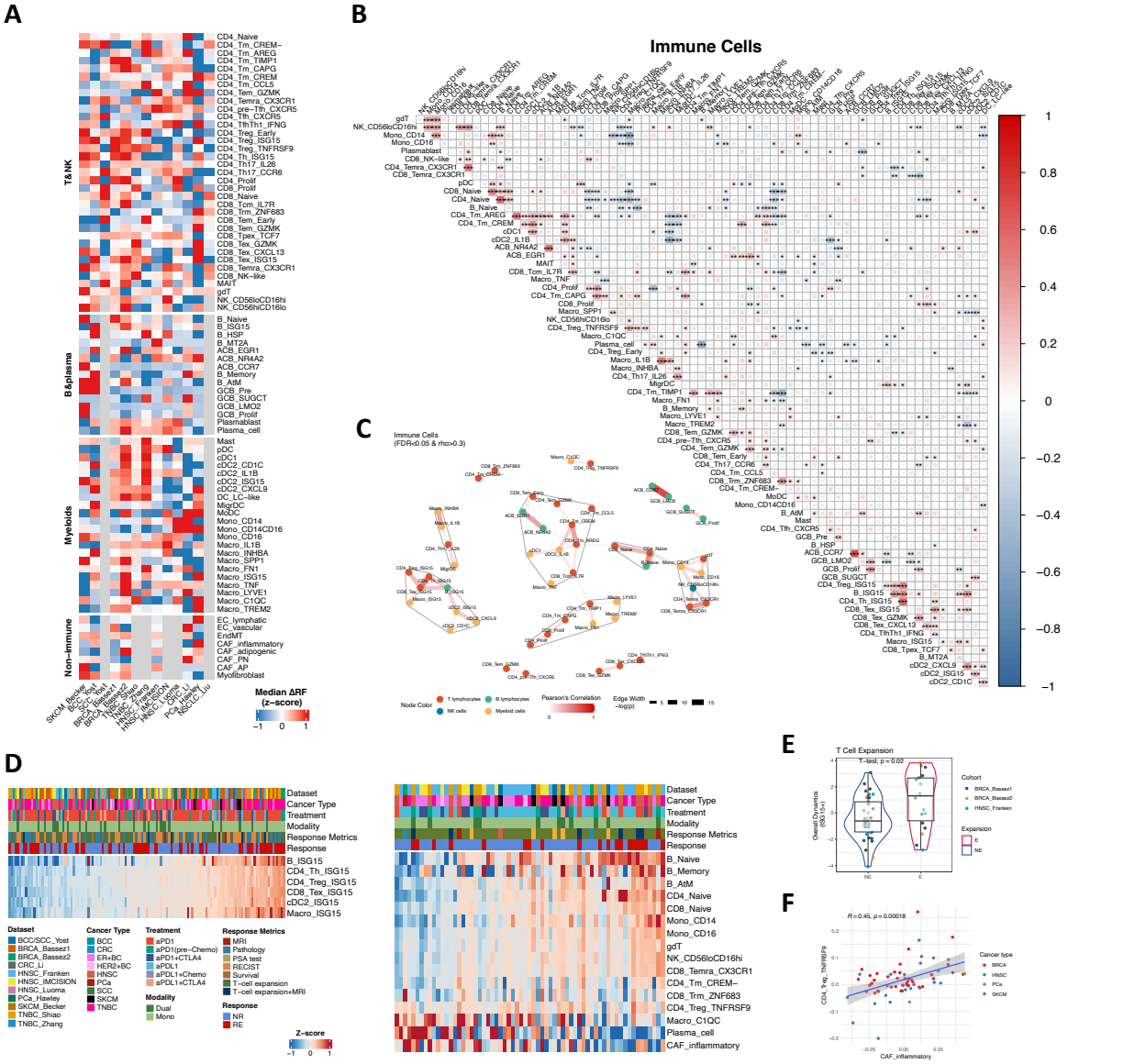

Figure 4. Co-regulating patterns upon ICI treatment. A. *Heatmap showing the median (row-wise scaled) proportion changes (Δrelative frequency, ΔRF) for cell types across cohorts. The gray color indicates that the cell type was absent from the cohort.* ***B.*** *Correlation matrix showing the pairwise Pearson correlations between dynamic changes (ΔRF) of immune cell types per patient, *p < 0.05, **p < 0.01, ***p < 0.001, based on the correlation.* ***C.*** *Undirected graph showing significant positive (FDR<0.05, Pearson's rho>0.3) correlations (edges) between cell types (nodes).* ***D.*** *Heatmap showing the coordinated switch among ISG15+ cell states (left) and a continuum from early activation/innate immune response to immune suppression (right). Patients (column) were sorted according to sum of corresponding cell type (row) dynamic changes.* ***E.*** *Box and violin plot comparing overall dynamics of ISG15+ cell subtypes between expanders and non-expanders. Boxes show 25th, median, and 75th percentiles.* ***F.*** *Scatter plot showing the correlation between TNFRSF9+ regulatory T cells and inflammatory cancer-associated fibroblasts based on the dynamic changes upon ICI treatment.*

Association of Immune Cell Dynamics with Treatment Response

We next performed a pairwise correlation analysis of cell state proportion changes in patients to identify groups exhibiting similar cellular dynamics in response to ICI treatment (**Figure 5A**). The resulting

correlation matrix facilitated the identification of three distinct patient clusters, with clusters 1 and 3 demonstrating particularly strong intra-group correlations and encompassing 42 and 45 patients, respectively. These clusters were found to display diametrically opposite dynamics, suggesting that the underlying cellular responses to ICI therapy were substantially different between the two groups.

This dichotomy in cellular dynamics was further substantiated by a significant association with treatment response; cluster 1 was enriched for responders (RE; 24 out of 42 patients), whereas cluster 3 consisted mainly of non-responders (NR; 31 out of 45 patients) (p-value = 0.026; **Figure 4B**). The association between cellular dynamics and treatment response was strengthened by the observation that similar correlation analyses performed solely on pre-treatment or post-treatment cell proportions did not yield clusters with a significant link to patient outcomes (**Figure S4A-D**). This finding emphasizes the significance of cellular dynamics, rather than static proportions at individual time points, as a determinant of patient response to ICI therapy.

The delineation of patient clusters based on treatment dynamics offers a compelling insight into the potential of cellular dynamics as a biomarker for ICI responsiveness. This dynamic-based patient stratification could prove to be a powerful tool in predicting treatment outcomes and tailoring therapy to individual patients. By examining the cell states mean dynamics across the clusters, we identified that cluster 1 (referred to RE-enriched) was enriched with interferon responsive states (B cells and cDC), components of tertiary lymphoid structure (TLS, naive CD4+T cells, CD4+Tfh cells, naive/memory/activated B cells, migrDC), and relevant precursors (CD4+ pre-Tfh, *CXCL9*+ cDC2) (**Figure 5C,D**). Cluster 3 (referred to NR-enriched) on the other hand was enriched with cell states associated with immune maturation and suppression, including plasma cells, MAIT, *TNFRSF9*+ Tregs, *C1QC*+ macrophages, etc.

To delineate the cellular determinants of treatment response, we performed a supervised subgroup analysis, dividing the aggregated cohort into responders and non-responders (**Figure 5E**). For cell states that showed coordinated dynamics between the two groups, *IL7R*+ CD8+ Tcm increased significantly in both groups, with a more pronounced increase in the NR group. In contrast, *GZMK*+ CD4+ Tem and activated/GC B cells showed more substantial increments in the RE group. For cell states that exhibited divergent trends, *TNFRSF*+ Tregs, *CCR6*+ CD4+ Th17 cells, and plasma cells displayed significant reductions in the RE group, while their increases in the NR group were not significant. Memory B cells and monocyte derived DCs exhibited significant increases in the RE group but not in the NR group. Conversely, the non-classical monocytes decreased significantly in the NR group but not in the RE group. Some cell states, such as *ISG15*+ cell states, displayed inconsistent trends compared to the unsupervised analysis, likely due to different response metrics in different studies. By further subdividing the group by datasets, we observed

similar trends, while most were not significant due to the limited sample sizes (**Figure 5F**). Highlighted by both unsupervised and supervised analysis, the increments of plasma cells and *TNFRSF+* Tregs, and *C1QC+* macrophages were correlated with adverse treatment response. These cell states may serve as potential biomarkers for patient stratification and could be investigated further for their mechanistic roles in mediating the efficacy of ICI therapy.

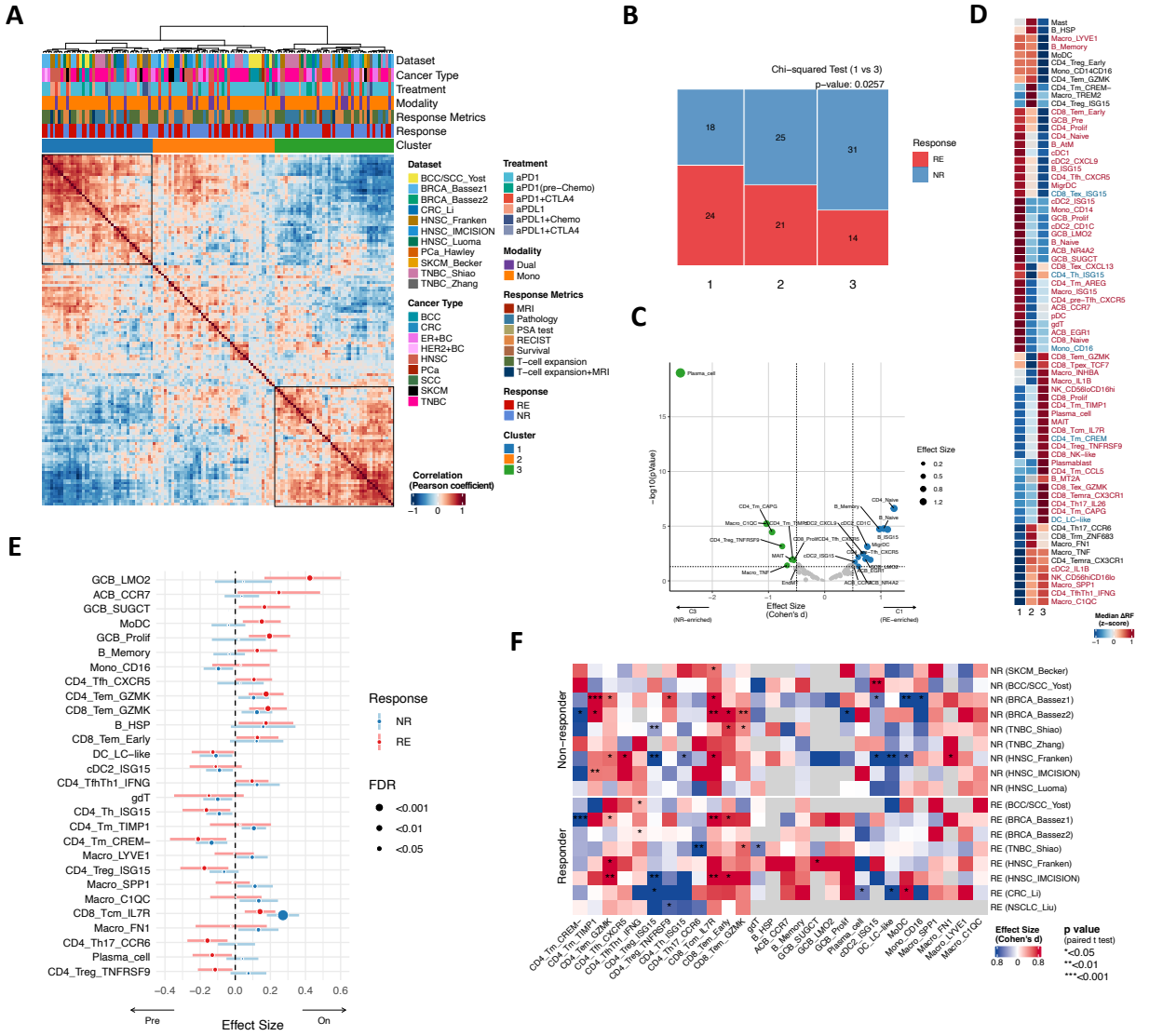

Figure 5. Association of Immune Cell Dynamics with Treatment Response. A*. Heatmap showing the pairwise Pearson correlation matrix across the patients according to the dynamics of immune cells.* ***B.*** *Mosaic plot showing numbers of responders and non-responders in dynamic-derived clusters.* ***C.*** *Volcano plot showing differential dynamics of immune cell dynamics between cluster 1 (responder-enriched) and cluster 3 (non-responder enriched), effect sizes were based on Cohen's d and p values were based on paired t-test.* ***D.*** *Heatmap showing the median dynamics (Δ relative frequency, row-wise scaled) of immune cell types (row) in the 3 clusters.* ***E.*** *Association between cell types and time points in responders and non-responders, the effect sizes (error bars indicate 95% confidence intervals) were based on the coefficients from linear mixed-effects models.* ***F.*** *Heatmap showing the effect sizes (Cohen's d) of compositional change for each cell types (column) in response-cohort subgroups (row), *p<0.05, **p<0.01, ***p<0.001, based on paired Student's t-test. Gray color indicates that the cell type detected in <3 patients from the subgroup.*

Discussion

We present a comprehensive analysis of cellular dynamics within the TME in response to ICI therapy across multiple cancer types. By leveraging a large-scale pan-cancer atlas of longitudinally paired ICI-treated tumors studied by sc-RNAseq, we provide novel insights into the complex interplay of immune and non-immune cells during ICI treatment and their relationship to treatment response.

One of the key technical contributions of our study is the development of a robust deep-phenotyping framework for accurate identification of cell types, subtypes, and functional states within the TME. Traditional clustering-based approaches often struggle with batch effects and generate impure clusters, leading to suboptimal cell type annotations. Annotating within individual studies can be challenging due to inconsistent annotation depth across studies. To overcome these limitations, we employed a two-step annotation process that minimizes reliance on data integration and clustering. By utilizing multiple reference datasets and carefully reviewing the annotations, our approach enables the identification of granular cell states with high purity and interpretability. Another important technical aspect of our study is the shift in the statistical unit of analysis from single cells to samples. While most single-cell studies focus on individual cells as the primary unit of analysis, connecting cellular dynamics to clinical outcomes, such as treatment response, requires a sample-level approach. However, as highlighted in our subgroup analysis, the small sample sizes in individual studies often limit the ability to detect relevant associations between cellular dynamics and clinical variables. By aggregating data from multiple studies with the pan-cancer TME annotation, our meta-analysis substantially increases the statistical power, enabling the identification of consistent evolution across datasets that may not be apparent in individual studies alone. This highlights the importance of collaborative efforts and data sharing in the single-cell research community to uncover biologically meaningful and clinically relevant patterns.

Our analysis revealed several key findings regarding the cellular dynamics within the TME upon ICI treatment. We observed a significant increase in immune subtypes, such as *IL7R*+ Tcm and *GZMK*+ Tem, CD4+ ThfTh1. However, these changes did not differ between patients under different treatments or between responders and non-responders. The addition of anti-CTLA4 significantly promoted the accumulation of pro-angiogenesis myeloid subtypes in head and neck cancer.

The co-regulating network analysis revealed a gradient of IFN-responsive cell states and a polarity in anti-tumor immune responses among patients. We found a global decrease in IFN-responsive states across immune components, but better responses when these states were retained. It should be noted that IFN-responsive immune subtypes were not consistently characterized across studies due to variations in T cell

annotation strategies, and some studies even regressed out the IFN signal during data scaling[20,24]. Our finding contrasts with studies in mice that blocking IFN signaling could resensitize resistant tumors[32,33] and a recent phase 2 trial for metastatic NSCLC that combined JAK inhibition with PD-1 immunotherapy to inhibit chronic IFN stimulation, which showed high response rates[34]. However, these analyses were based on sorted CD8+ T cells from pooled blood and tumor tissue samples without specific ISG+ subset characterization. These differences in sample sources and annotation strategies highlight the complexity of understanding the dynamics and impact of the IFN response in the TME upon ICI treatment.

Our results however align with recent pan-cancer studies that identified the IFN-enriched network in correlation with a favorable response[2,35]. The coordinated regulation of the IFN-responsive immune components was further confirmed to correlate with TME response in terms of T cell expansion. Although there remains a gap between T cell expansion and actual clinical benefit, the mechanism by which this impacts treatment response warrants further investigation. The transition involving adaptive and innate immune cells, along with immune and non-immune components, demonstrates a polarity from an initial immune status for antigen engagement and initiation of adaptive immune responses towards the modulation of immune activation and the establishment of an immunosuppressive environment. This transition is marked by a notable reduction in treatment response.

The role of compositional changes in response prediction across cancer types remained largely unknown. We identified distinct patient clusters based on the dynamics, with one cluster enriched for responders and another enriched for non-responders. This dynamic-based patient stratification suggests that the underlying cellular responses to ICI therapy may serve as a potential biomarker for predicting treatment outcomes. Resembling the co-regulated transition, the RE-enriched cluster, which includes additional TLS components and IFN-responsive subtypes, is more dominated by the initiated anti-tumor responses. In contrast, the NR-enriched cluster possesses a more well-established and immunosuppressive environment. The response-based subgroup analysis further confirmed the preferential accumulation of plasma cells and *TNFRSF9*+ Treg in the non-responders.

While our deep-phenotyping approach represents an improvement over existing methods, it is important to acknowledge the inherent challenges in delineating cell states within the TME. The continuum of cell states and the subtle differences between them make it difficult to establish clear boundaries, even with advanced analytical techniques. This notion underscores the complexity of the biological system and the need for further refinement of computational methods to better capture the nuances of cellular heterogeneity. Another limitation of our study is the heterogeneity in response metrics across studies, which may introduce some variability in the associations between cellular dynamics and treatment outcomes. Future efforts to

standardize response criteria and harmonize data collection across institutions should further improve the reliability and robustness of such meta-analyses.

In conclusion, our analysis presents a distinct perspective in addressing inter-sample variation of large-scale longitudinally paired scRNA-seq cohort, by treating samples as statistical replication. Through compositional comparison, it provides a panoramic view of the cellular composition dynamics within the TME during ICI therapy across multiple cancer types. The granular annotation by the proposed robust deep-phenotyping framework facilitated the identification of co-regulated cell communities that may govern the efficacy of ICI therapy. These findings highlight the importance of a systematic approach to understanding the complex interplay within the TME and pave the way for the development of more effective immunotherapeutic strategies. Future studies building upon these results will further elucidate the mechanisms underlying treatment response and resistance, ultimately leading to improved patient stratification and personalized cancer immunotherapy.

Methods

Single-cell RNA-seq data curation and standardization

We curated and standardized longitudinal paired transcriptomic data from 141 patients undergoing immunotherapy with immune checkpoint inhibitors (ICIs), encompassing 10 cancer subtypes across 12 cohorts from 11 independent datasets (**Table S1**). Among these, one was internally generated at the University Hospital Essen, specifically within the Departments of Translational Skin Cancer Research and Dermatology. Additionally, we supplemented our data with public datasets, identified through an extensive literature review conducted up to March 2024.

The interval between the initiation of treatment and the collection of the second sample was categorized into two groups: less than 21 days (early on) and 21 days or more (late on). Treatment regimens were classified based on their composition into several categories: anti-PD-1 (aPD1), anti-PD-1 before chemotherapy [aPD1(pre-Chemo)], anti-PD-1 combined with chemotherapy (aPD1+Chemo), anti-PD-1 combined with CTLA-4 inhibition (aPD1+CTLA4), anti-PD-L1 (aPDL1), anti-PD-L1 combined with chemotherapy (aPDL1+Chemo), and anti-PD-L1 combined with CTLA-4 inhibition (aPDL1+CTLA4). These were further grouped into monotherapy and dual therapy based on the checkpoint antibodies used.

Due to the heterogeneity in study designs across datasets, response metrics varied, incorporating methods like early/standard radiological assessment (MRI/RECIST), blood tests (PSA), T-cell expansion (scTCR-seq), and clinical outcomes (survival). The classification of patients as responders in our analysis adopts

the criteria used in their respective original studies. An exception is made for the HNSC_Franken cohort, where only those patients who did not exhibit tumor growth were categorized as responders in our study.

Single-cell RNA-seq Data preprocessing

Newly generated single-cell sequencing data were aligned with the GRCh38 human reference genome and quantified using Cell Ranger (version 3.0, 10x Genomics Inc). The quality of cells was assessed based on two metrics: (1) The number of detected genes per cell; and (2) The proportion of mitochondrial gene counts per cell. Specifically, cells with detected genes fewer than 200 or greater than 6000, and mitochondrial unique molecular identifier (UMI) count percentage larger than 20% were filtered out. The genes detected in more than 3 cells were retained. To remove the potential doublets, scDblFinder[36] and DoubletFinder[37] were used for each sequencing library with the expected doublet rate set to be 0.08, and cells identified as doublets by both methods were further filtered out. For each dataset, gene symbols were converted into a common dictionary with STACAS:::standardizeGeneSymbols()[38].

After the removal of low-quality cells and deep phenotyping, sample-level quality control was applied to remove samples with fewer than 200 non-cancer cells or less than 9000 detected genes.

Single-cell RNA-seq Annotation

The annotation of single-cell RNA-seq data is performed at 2 levels, built on the reference-based SingleR annotation tool. At Level 1, cells are divided into discrete lineage populations. Level 2 focuses on the annotation of cells to the most granular cell types/states.

Level 1 starts with the assignment of major lineage components utilizing SingleR[30] with the BlueprintEncodeData[39,40] as a reference and using the built-in pruning approach in SingleR. The pruning will cause low-quality assignments to not be labeled. To assign those low-quality cells, we utilized the scGate[29]. First, we integrated all the data with Harmony[41] and clustered with Seurat[42] with a resolution of 0.5. Unknown cell types were then annotated using scGate with a pre-defined multi-classifier (TME_HiRes). Plasmacytoid dendritic cells (pDC) were isolated by the positive expression of *LILRA4* and *JCHAIN*. Mixed cell types, including non-immune cells present in the CD45+ sorted data and cells identified as multi-label by scGate, were filtered out. Additionally, due to the technical limitations of 10X sequencing, the neutrophils were also excluded from further analysis. At the end of this step, cells are classified into major groups, including T and NK cells, myeloid cells, B lymphocytes, endothelial cells, and fibroblasts.

Level 2 annotations were designed to cater to various cellular lineages, and consists of two primary steps - preparation of reference sets and subsequent deep phenotyping:

Reference preparation. The reference data for T-cells, NK cells, myeloid cells, and CAFs were retrieved from the pan-cancer atlas studies[17,43-46], loaded in R as SingleCellExperiment objects, and processed individually. The objects were split by cancer types as lists, normalized with logNormCounts() function, and further aggregated into pseudo-bulk samples aggregateReference() function by the granular level labels from original studies. Additionally, to capture the diversity of main components, data for T cells, myeloid cells, and B lymphocytes were aggregated at the main level (e.g., CD4+ T cells, CD8+ T cells, cDC, macrophages, B cells, plasma cells) to ensure accurate intra-lineage reclassification. Due to the relatively lower abundance, the reference data of NK cells was aggregated only at the main level ($CD56^{high}CD16^{low}$, $CD56^{high}CD16^{high}$, and $CD56^{low}CD16^{high}$). The endothelial cell reference data was derived from the HPV-negative head and neck cancer dataset[47], by manual annotation with Seurat pipeline, then aggregated as aforementioned.

Deep phenotyping. Immune cells were first classified into main cell types within each lineage by SingleR based on the pan-cancer reference at the main level. For the T and NK cell group, this included CD4+ T cells, CD8+ T cells, and NK cells. For the myeloid cells group, this included cDCs, monocytes, and macrophages. For the B lymphocytes, this included B cells, GC B cells, and plasma cells.

Due to the distinct marker expression, the scGate was applied to separate cells from the T and NK cells group, with *KLRD1* and *NCAM1* served as positive markers, and CD3D as a negative marker for NK cells, and *CD3D*, *TRGC2*, *TRDV2*, *TRGV9*, *TRGV10*, and *TRDC* as positive markers, and CD8A and CD4 as negative markers for the gdT cells. After separating the NK and gd T cells, the remaining CD4+/CD8+ T cells underwent further 'gating' by the generic CD4T and CD8T models from scGate. Cells with overlapped labels were identified by SingleR, based on an aggregated pan-cancer reference at the main level. Following the main-level annotation, the immune cells were further annotated within each main cell type by SingleR with pan-cancer reference at the deep level.

Non-immune cells including endothelial cells and fibroblasts cells were annotated directly to the deep level by using SingleR with corresponding reference.

After prediction, the labels were manually adjusted according to the extensively updated markers.

Cell Type Composition

Based on the annotation, cellular composition (referred as the relative frequency, RF) was calculated within each major group, including T and NK cells, B and plasma cells, myeloid cells, and non-immune cells. The change in RF was calculated by subtracting the relative frequency at baseline from the RF at the second time point.

Linear Mixed Effects Models

Dynamic changes in functional pathways and composition during the treatment were evaluated using mixed effects regression models with the lmerTest package[48]. These models were adjusted for factors such as dataset, sample collection interval, and treatment modality, incorporating individual patients as random effects to account for the paired sample design. P values were adjusted for the false discovery rate (FDR) to control for multiple comparisons in the analysis.

Cell Type-specific Gene Set Enrichment

Gene set enrichment scoring was conducted using the UCell[49], which is based on the relative ranking of genes for individual cells, robust to dataset composition. T cell-specific signatures, encompassing differentiation, function, metabolism, and apoptosis for both CD4+ and CD8+ T cells, were derived from an earlier pan-cancer T cell analysis. For macrophages, gene sets including KEGG's antigen processing and presentation, along with hallmark pathways such as interferon-gamma response, complement, and TNFα signaling via NFκB, were retrieved via the msigdbr package[50]. Additionally, the M1, M2, angiogenesis, and phagocytosis signatures from a previous pan-cancer myeloid cell study were incorporated.

Differential Expression Analysis and Over-representation Enrichment Analysis

The differential expression analysis was performed by using rank_genes_groups() function from the scanpy package based on the Wilcoxon rank-sum test. P-values were corrected by Benjamini–Hochberg method. Genes with adjusted p-values < 0.05 were included in functional enrichment analysis. The functional enrichment analysis was performed by using the GSEApy package[51] with the MSigDB_Hallmark library[52]. The enriched pathways with overlapping genes $\leq 50\%$ were filtered out.

Unsupervised Clustering

The correlation analysis was performed using Pearson correlation test. The unsupervised hierarchical clustering and heatmap visualization were performed based on the Euclidean distance of correlation by the corrplot[53] and ComplexHeatmap[54] R packages.

Statistical Analysis

All statistical analyses were performed in R software 4.3.0 and Python 3.9. The evenness of relative frequencies for cell subtypes at a single time-point was calculated with the Shannon equitability index, which ranges from 0 to 1 (complete evenness). Comparisons between two groups were performed using

either a two-tailed paired Student's t-test (unless otherwise indicated), and the effect size was calculated with Cohen's d. The statistical significance was set to p-value < 0.05, The other statistical methods for specific analyses are present in the sections above.

Data availability

All single-cell data are available from the corresponding studies (**Table S1**). The Becker dataset was deposited at the European Genome-Phenome Archive (EGA, awaiting approval).

Code availability

The code for reproducing all the analyses in the study is available at https://github.com/zlin-bioinfo/Pan-cancer_ICI.

Acknowledgments

This work was funded by the Israel Science Foundation (1543/21) and Azrieli Faculty Fellowship (to DA), by Deutsches Konsortium für Translationale Krebsforschung (ED03 to JCB) and Else-Kröner-Fresenius Stiftung (EFKS), University Medicine Essen Medical Scientist Academy (UMESciA) (to NS).

Declaration of interests

JCB is receiving speaker's bureau honoraria from Amgen, Pfizer, Recordati and Sanofi, is a paid consultant/advisory board member/DSMB member for Almirall, Boehringer Ingelheim, InProTher, ICON, MerckSerono, Pfizer, Regeneron, 4SC, and Sanofi. His group receives research grants from Merck Serono, HTG, IQVIA, and Alcedis. DA is a consultant to Carelon Digital Platforms and Link Cell Therapies. All other authors declare no competing financial interests.

Author contributions

DA and JCB conceived the study and supervised the analyses. ZL performed all bioinformatics analyses. EP provided bioinformatics support. MC and NS performed the sc-RNA-seq. SU collected the samples from the patients. DA and ZL wrote the manuscript with inputs from JCB.

References

1. Shaked, Y. (2016). Balancing efficacy of and host immune responses to cancer therapy: the yin and yang effects. Nat Rev Clin Oncol *13*, 611-626. 10.1038/nrclinonc.2016.57.
2. Thorsson, V., Gibbs, D.L., Brown, S.D., Wolf, D., Bortone, D.S., Ou Yang, T.H., Porta-Pardo, E., Gao, G.F., Plaisier, C.L., Eddy, J.A., et al. (2018). The Immune Landscape of Cancer. Immunity *48*, 812-830 e814. 10.1016/j.immuni.2018.03.023.
3. Ren, X., Zhang, L., Zhang, Y., Li, Z., Siemers, N., and Zhang, Z. (2021). Insights Gained from Single-Cell Analysis of Immune Cells in the Tumor Microenvironment. Annu Rev Immunol *39*, 583-609. 10.1146/annurev-immunol-110519-071134.
4. Rood, J.E., Maartens, A., Hupalowska, A., Teichmann, S.A., and Regev, A. (2022). Impact of the Human Cell Atlas on medicine. Nat Med *28*, 2486-2496. 10.1038/s41591-022-02104-7.
5. Hodi, F.S., O'Day, S.J., McDermott, D.F., Weber, R.W., Sosman, J.A., Haanen, J.B., Gonzalez, R., Robert, C., Schadendorf, D., Hassel, J.C., et al. (2010). Improved Survival with Ipilimumab in Patients with Metastatic Melanoma. New England Journal of Medicine *363*, 711-723. doi:10.1056/NEJMoa1003466.
6. Brahmer, J.R., Tykodi, S.S., Chow, L.Q.M., Hwu, W.-J., Topalian, S.L., Hwu, P., Drake, C.G., Camacho, L.H., Kauh, J., Odunsi, K., et al. (2012). Safety and Activity of Anti–PD-L1 Antibody in Patients with Advanced Cancer. New England Journal of Medicine *366*, 2455-2465. doi:10.1056/NEJMoa1200694.
7. Ribas, A., and Wolchok, J.D. (2018). Cancer immunotherapy using checkpoint blockade. Science *359*, 1350-1355. doi:10.1126/science.aar4060.
8. Wolchok, J.D., Chiarion-Sileni, V., Gonzalez, R., Grob, J.-J., Rutkowski, P., Lao, C.D., Cowey, C.L., Schadendorf, D., Wagstaff, J., Dummer, R., et al. (2022). Long-Term Outcomes With Nivolumab Plus Ipilimumab or Nivolumab Alone Versus Ipilimumab in Patients With Advanced Melanoma. Journal of Clinical Oncology *40*, 127-137. 10.1200/jco.21.02229.
9. Huang, A.C., and Zappasodi, R. (2022). A decade of checkpoint blockade immunotherapy in melanoma: understanding the molecular basis for immune sensitivity and resistance. Nature Immunology *23*, 660-670. 10.1038/s41590-022-01141-1.
10. Motzer, R.J., Rini, B.I., McDermott, D.F., Redman, B.G., Kuzel, T.M., Harrison, M.R., Vaishampayan, U.N., Drabkin, H.A., George, S., Logan, T.F., et al. (2015). Nivolumab for Metastatic Renal Cell Carcinoma: Results of a Randomized Phase II Trial. Journal of Clinical Oncology *33*, 1430-1437. 10.1200/jco.2014.59.0703.
11. Topalian, S.L., Hodi, F.S., Brahmer, J.R., Gettinger, S.N., Smith, D.C., McDermott, D.F., Powderly, J.D., Carvajal, R.D., Sosman, J.A., Atkins, M.B., et al. (2012). Safety, Activity, and Immune Correlates of Anti–PD-1 Antibody in Cancer. New England Journal of Medicine *366*, 2443-2454. doi:10.1056/NEJMoa1200690.
12. Boutros, C., Tarhini, A., Routier, E., Lambotte, O., Ladurie, F.L., Carbonnel, F., Izzeddine, H., Marabelle, A., Champiat, S., Berdelou, A., et al. (2016). Safety profiles of anti-CTLA-4 and anti-PD-1 antibodies alone and in combination. Nat Rev Clin Oncol *13*, 473-486. 10.1038/nrclinonc.2016.58.
13. Lauss, M., Donia, M., Harbst, K., Andersen, R., Mitra, S., Rosengren, F., Salim, M., Vallon-Christersson, J., Törngren, T., Kvist, A., et al. (2017). Mutational and putative neoantigen load predict clinical benefit of adoptive T cell therapy in melanoma. Nature Communications *8*, 1738. 10.1038/s41467-017-01460-0.
14. Galon, J., and Bruni, D. (2019). Approaches to treat immune hot, altered and cold tumours with combination immunotherapies. Nature Reviews Drug Discovery *18*, 197-218. 10.1038/s41573-018-0007-y.

15. Bagaev, A., Kotlov, N., Nomie, K., Svekolkin, V., Gafurov, A., Isaeva, O., Osokin, N., Kozlov, I., Frenkel, F., Gancharova, O., et al. (2021). Conserved pan-cancer microenvironment subtypes predict response to immunotherapy. Cancer Cell *39*, 845-865 e847. 10.1016/j.ccell.2021.04.014.
16. Qian, J., Olbrecht, S., Boeckx, B., Vos, H., Laoui, D., Etlioglu, E., Wauters, E., Pomella, V., Verbandt, S., Busschaert, P., et al. (2020). A pan-cancer blueprint of the heterogeneous tumor microenvironment revealed by single-cell profiling. Cell Res *30*, 745-762. 10.1038/s41422-020-0355-0.
17. Zheng, L., Qin, S., Si, W., Wang, A., Xing, B., Gao, R., Ren, X., Wang, L., Wu, X., Zhang, J., et al. (2021). Pan-cancer single-cell landscape of tumor-infiltrating T cells. Science *374*, abe6474. 10.1126/science.abe6474.
18. Yost, K.E., Satpathy, A.T., Wells, D.K., Qi, Y., Wang, C., Kageyama, R., McNamara, K.L., Granja, J.M., Sarin, K.Y., Brown, R.A., et al. (2019). Clonal replacement of tumor-specific T cells following PD-1 blockade. Nat Med *25*, 1251-1259. 10.1038/s41591-019-0522-3.
19. Liu, B., Hu, X., Feng, K., Gao, R., Xue, Z., Zhang, S., Zhang, Y., Corse, E., Hu, Y., Han, W., and Zhang, Z. (2022). Temporal single-cell tracing reveals clonal revival and expansion of precursor exhausted T cells during anti-PD-1 therapy in lung cancer. Nat Cancer *3*, 108-121. 10.1038/s43018-021-00292-8.
20. Bassez, A., Vos, H., Van Dyck, L., Floris, G., Arijs, I., Desmedt, C., Boeckx, B., Vanden Bempt, M., Nevelsteen, I., Lambein, K., et al. (2021). A single-cell map of intratumoral changes during anti-PD1 treatment of patients with breast cancer. Nat Med *27*, 820-832. 10.1038/s41591-021-01323-8.
21. Zhang, Y., Chen, H., Mo, H., Hu, X., Gao, R., Zhao, Y., Liu, B., Niu, L., Sun, X., Yu, X., et al. (2021). Single-cell analyses reveal key immune cell subsets associated with response to PD-L1 blockade in triple-negative breast cancer. Cancer Cell *39*, 1578-1593 e1578. 10.1016/j.ccell.2021.09.010.
22. van der Leun, A.M., Traets, J.J.H., Vos, J.L., Elbers, J.B.W., Patiwael, S., Qiao, X., Machuca-Ostos, M., Thommen, D.S., Haanen, J., Schumacher, T.N.M., and Zuur, C.L. (2023). Dual Immune Checkpoint Blockade Induces Analogous Alterations in the Dysfunctional CD8+ T-cell and Activated Treg Compartment. Cancer Discov *13*, 2212-2227. 10.1158/2159-8290.CD-22-0851.
23. Li, J., Wu, C., Hu, H., Qin, G., Wu, X., Bai, F., Zhang, J., Cai, Y., Huang, Y., Wang, C., et al. (2023). Remodeling of the immune and stromal cell compartment by PD-1 blockade in mismatch repair-deficient colorectal cancer. Cancer Cell. 10.1016/j.ccell.2023.04.011.
24. Franken, A., Bila, M., Mechels, A., Kint, S., Van Dessel, J., Pomella, V., Vanuytven, S., Philips, G., Bricard, O., Xiong, J., et al. (2024). CD4+ T cell activation distinguishes response to anti-PD-L1+anti-CTLA4 therapy from anti-PD-L1 monotherapy. Immunity. 10.1016/j.immuni.2024.02.007.
25. Shiao, S.L., Gouin, K.H., 3rd, Ing, N., Ho, A., Basho, R., Shah, A., Mebane, R.H., Zitser, D., Martinez, A., Mevises, N.Y., et al. (2024). Single-cell and spatial profiling identify three response trajectories to pembrolizumab and radiation therapy in triple negative breast cancer. Cancer Cell *42*, 70-84 e78. 10.1016/j.ccell.2023.12.012.
26. Luoma, A.M., Suo, S., Wang, Y., Gunasti, L., Porter, C.B.M., Nabilsi, N., Tadros, J., Ferretti, A.P., Liao, S., Gurer, C., et al. (2022). Tissue-resident memory and circulating T cells are early responders to pre-surgical cancer immunotherapy. Cell *185*, 2918-2935 e2929. 10.1016/j.cell.2022.06.018.
27. Hawley, J.E., Obradovic, A.Z., Dallos, M.C., Lim, E.A., Runcie, K., Ager, C.R., McKiernan, J., Anderson, C.B., Decastro, G.J., Weintraub, J., et al. (2023). Anti-PD-1 immunotherapy with androgen deprivation therapy induces robust immune infiltration in metastatic castration-sensitive prostate cancer. Cancer Cell. 10.1016/j.ccell.2023.10.006.

28. Li, B., Cui, Y., Diehn, M., and Li, R. (2017). Development and Validation of an Individualized Immune Prognostic Signature in Early-Stage Nonsquamous Non-Small Cell Lung Cancer. JAMA Oncol *3*, 1529-1537. 10.1001/jamaoncol.2017.1609.
29. Andreatta, M., Berenstein, A.J., and Carmona, S.J. (2022). scGate: marker-based purification of cell types from heterogeneous single-cell RNA-seq datasets. Bioinformatics *38*, 2642-2644. 10.1093/bioinformatics/btac141.
30. Aran, D., Looney, A.P., Liu, L., Wu, E., Fong, V., Hsu, A., Chak, S., Naikawadi, R.P., Wolters, P.J., Abate, A.R., et al. (2019). Reference-based analysis of lung single-cell sequencing reveals a transitional profibrotic macrophage. Nat Immunol *20*, 163-172. 10.1038/s41590-018-0276-y.
31. Traag, V.A., Waltman, L., and van Eck, N.J. (2019). From Louvain to Leiden: guaranteeing well-connected communities. Scientific Reports *9*, 5233. 10.1038/s41598-019-41695-z.
32. Chen, W., Teo, J.M.N., Yau, S.W., Wong, M.Y.-M., Lok, C.-N., Che, C.-M., Javed, A., Huang, Y., Ma, S., and Ling, G.S. (2022). Chronic type I interferon signaling promotes lipid-peroxidation-driven terminal CD8+ T cell exhaustion and curtails anti-PD-1 efficacy. Cell Reports *41*, 111647. https://doi.org/10.1016/j.celrep.2022.111647.
33. Benci, J.L., Johnson, L.R., Choa, R., Xu, Y., Qiu, J., Zhou, Z., Xu, B., Ye, D., Nathanson, K.L., June, C.H., et al. (2019). Opposing Functions of Interferon Coordinate Adaptive and Innate Immune Responses to Cancer Immune Checkpoint Blockade. Cell *178*, 933-948.e914. https://doi.org/10.1016/j.cell.2019.07.019.
34. Mathew, D., Marmarelis, M.E., Foley, C., Bauml, J.M., Ye, D., Ghinnagow, R., Ngiow, S.F., Klapholz, M., Jun, S., Zhang, Z., et al. (2024). Combined JAK inhibition and PD-1 immunotherapy for non–small cell lung cancer patients. Science *384*. 10.1126/science.adf1329.
35. Kang, J., Lee, J.H., Cha, H., An, J., Kwon, J., Lee, S., Kim, S., Baykan, M.Y., Kim, S.Y., An, D., et al. (2024). Systematic dissection of tumor-normal single-cell ecosystems across a thousand tumors of 30 cancer types. Nat Commun *15*, 4067. 10.1038/s41467-024-48310-4.
36. Germain, P.-L., Lun, A., Garcia Meixide, C., Macnair, W., and Robinson, M.D. (2022). Doublet identification in single-cell sequencing data using scDblFinder. F1000Research *10*, 979. 10.12688/f1000research.73600.2.
37. McGinnis, C.S., Murrow, L.M., and Gartner, Z.J. (2019). DoubletFinder: Doublet Detection in Single-Cell RNA Sequencing Data Using Artificial Nearest Neighbors. Cell Systems *8*, 329-337.e324. 10.1016/j.cels.2019.03.003.
38. Andreatta, M., Hérault, L., Gueguen, P., Gfeller, D., Berenstein, A.J., and Carmona, S.J. (2024). Semi-supervised integration of single-cell transcriptomics data. Nature Communications *15*, 872. 10.1038/s41467-024-45240-z.
39. Stunnenberg, H.G., Abrignani, S., Adams, D., de Almeida, M., Altucci, L., Amin, V., Amit, I., Antonarakis, S.E., Aparicio, S., Arima, T., et al. (2016). The International Human Epigenome Consortium: A Blueprint for Scientific Collaboration and Discovery. Cell *167*, 1145-1149. https://doi.org/10.1016/j.cell.2016.11.007.
40. Dunham, I., Kundaje, A., Aldred, S.F., Collins, P.J., Davis, C.A., Doyle, F., Epstein, C.B., Frietze, S., Harrow, J., Kaul, R., et al. (2012). An integrated encyclopedia of DNA elements in the human genome. Nature *489*, 57-74. 10.1038/nature11247.
41. Korsunsky, I., Millard, N., Fan, J., Slowikowski, K., Zhang, F., Wei, K., Baglaenko, Y., Brenner, M., Loh, P.R., and Raychaudhuri, S. (2019). Fast, sensitive and accurate integration of single-cell data with Harmony. Nat Methods *16*, 1289-1296. 10.1038/s41592-019-0619-0.
42. Hao, Y., Stuart, T., Kowalski, M.H., Choudhary, S., Hoffman, P., Hartman, A., Srivastava, A., Molla, G., Madad, S., Fernandez-Granda, C., and Satija, R. (2023). Dictionary learning for integrative, multimodal and scalable single-cell analysis. Nat Biotechnol. 10.1038/s41587-023-01767-y.
43. Tang, F., Li, J., Qi, L., Liu, D., Bo, Y., Qin, S., Miao, Y., Yu, K., Hou, W., Li, J., et al. (2023). A pan-cancer single-cell panorama of human natural killer cells. Cell. 10.1016/j.cell.2023.07.034.

44. Cheng, S., Li, Z., Gao, R., Xing, B., Gao, Y., Yang, Y., Qin, S., Zhang, L., Ouyang, H., Du, P., et al. (2021). A pan-cancer single-cell transcriptional atlas of tumor infiltrating myeloid cells. Cell *184*, 792-809 e723. 10.1016/j.cell.2021.01.010.
45. Ma, J., Wu, Y., Ma, L., Yang, X., Zhang, T., Song, G., Li, T., Gao, K., Shen, X., Lin, J., et al. (2024). A blueprint for tumor-infiltrating B cells across human cancers. Science *384*, eadj4857. 10.1126/science.adj4857.
46. Luo, H., Xia, X., Huang, L.-B., An, H., Cao, M., Kim, G.D., Chen, H.-N., Zhang, W.-H., Shu, Y., Kong, X., et al. (2022). Pan-cancer single-cell analysis reveals the heterogeneity and plasticity of cancer-associated fibroblasts in the tumor microenvironment. Nature Communications *13*. 10.1038/s41467-022-34395-2.
47. Kurten, C.H.L., Kulkarni, A., Cillo, A.R., Santos, P.M., Roble, A.K., Onkar, S., Reeder, C., Lang, S., Chen, X., Duvvuri, U., et al. (2021). Investigating immune and non-immune cell interactions in head and neck tumors by single-cell RNA sequencing. Nat Commun *12*, 7338. 10.1038/s41467-021-27619-4.
48. Kuznetsova, A., Brockhoff, P.B., and Christensen, R.H.B. (2017). lmerTest Package: Tests in Linear Mixed Effects Models. Journal of Statistical Software *82*, 1 - 26. 10.18637/jss.v082.i13.
49. Andreatta, M., and Carmona, S.J. (2021). UCell: Robust and scalable single-cell gene signature scoring. Computational and Structural Biotechnology Journal *19*, 3796-3798. https://doi.org/10.1016/j.csbj.2021.06.043.
50. Dolgalev, I. (2022). msigdbr: MSigDB Gene Sets for Multiple Organisms in a Tidy Data Format.
51. Fang, Z., Liu, X., and Peltz, G. (2022). GSEApy: a comprehensive package for performing gene set enrichment analysis in Python. Bioinformatics *39*. 10.1093/bioinformatics/btac757.
52. Castanza, A.S., Recla, J.M., Eby, D., Thorvaldsdóttir, H., Bult, C.J., and Mesirov, J.P. (2023). Extending support for mouse data in the Molecular Signatures Database (MSigDB). Nature Methods *20*, 1619-1620. 10.1038/s41592-023-02014-7.
53. Simko, T.W.a.V. (2021). R package 'corrplot': Visualization of a Correlation Matrix.
54. Gu, Z. (2022). Complex heatmap visualization. iMeta *1*, e43. https://doi.org/10.1002/imt2.43.